

## RESEARCH ARTICLE

10.1002/2015JC011149

## Global C-Band Envisat, RADARSAT-2 and Sentinel-1 SAR measurements in copolarization and cross-polarization

A. Mouche<sup>1</sup> and B. Chapron<sup>1</sup><sup>1</sup>Laboratoire d'Océanographie Spatiale, Ifremer, Plouzané, France

## Key Points:

- First C-Band GMF in VV and HH and signals in cross-polarization from Sentinel-1 A are presented
- Results unify major findings from literature for polarization combination and cross-polarization
- Comparable wind sensitivity for cross-pol and HH crosswind signals is attributed to breaking events

## Correspondence to:

A. Mouche,  
amouche@ifremer.fr

## Citation:

Mouche, A., and B. Chapron (2015), Global C-Band Envisat, RADARSAT-2 and Sentinel-1 SAR measurements in copolarization and cross-polarization, *J. Geophys. Res. Oceans*, 120, 7195–7207, doi:10.1002/2015JC011149.

Received 17 JUL 2015

Accepted 5 OCT 2015

Accepted article online 23 OCT 2015

Published online 6 NOV 2015

**Abstract** Using colocated ASCAT and ECMWF winds, a careful global analysis of ENVISAT and Sentinel-1 synthetic aperture radar (SAR) measurements helps to refine, at medium resolution (tens of kilometers) and especially for HH configuration, a C-band geophysical model function (GMF, i.e., C-SARMOD) to analyze wind sensitivity for different incidence and azimuth angles. Results unify major findings from previous global and case studies for polarization ratio (PR, VV/HH), polarization difference (PD, VV-HH), and cross-polarization (CP). At lower level than standard two-scale predictions, PR increases with increasing incidence angle and decreases with increasing wind speed. PR further exhibits a strong azimuthal modulation, with maximum values in downwind configurations. The PD azimuth modulation is found more pronounced for VV than HH (VV being larger than HH), reaching maximum values for wind speed about 10 m/s. CP signals decrease with incidence angle but increase with wind speed, especially beyond 10 m/s, with no evidence of saturation. Remarkably, this also applies to HH crosswind measurements. This comparable high wind sensitivity for both CP and HH crosswind signals, with a clear departure from PD ones, can be related to the onset of vigorous breaking events, large enough to impact in-plane and out-of-plane local tilts. Considering that VV polarization best maximizes the polarized resonant contribution, combined CP and VV wide swath SAR observations can thus have the potential to efficiently map and contrast local directional aspects.

## 1. Introduction

With the advent of new spaceborne systems, especially synthetic aperture radar (SAR) dual-polarization and quad-polarization instruments, more detailed information on the surface signatures of high-resolution ocean-atmosphere processes is becoming available. For almost 10 years (2002–2012), ENVISAT ASAR provided large amount of high quality wide swath C-band radar images in vertical (VV) or horizontal (HH) copolarization, illustrating the potential to resolve fine-scale atmospheric and oceanic features, as well as to interpret and possibly exploit the estimated overall scatter line-of-sight velocity [Chapron *et al.*, 2005; Mouche *et al.*, 2008, 2012; Alpers *et al.*, 2015]. With extended polarization capabilities, including cross-polarized (CP) signals, RadarSAT-2 (RS-2), launched in 2007, further helped to reveal that CP radar backscatter signals are strongly sensitive to high wind conditions [e.g., Vachon and Wolfe, 2011; Hwang *et al.*, 2010a, 2010b; Zhang and Perrie, 2012]. Predominantly attributed to the breaking wave contributions [Hwang *et al.*, 2010a, 2010b], this opens new perspectives for the forthcoming generation of EPS-SG (EUMETSAT Polar System - Second Generation) ocean wind scatterometers [Lin *et al.*, 2012], as copolarization backscatter signals saturate under extreme wind conditions [e.g., Quilfen *et al.*, 2007].

Still for light to moderate wind conditions, the polarization sensitivity, especially the linear difference between VV and HH (PD), is compared to copolarized measurements, more directly governed by resonant scattering mechanism effects related to short and small amplitude surface scales. As the relaxation scale of centimeter-scale ocean surface scatters is rather small, from 10 to 100 m, this polarization sensitivity from PD contrasts can then appear distinct compared to VV, HH or polarization ratio (ratio of copolarized channels in natural unit, PR). This provides means to quantitatively interpret the surface manifestations related to ocean surface currents, slick and rapid local wind magnitude, and direction changes [Kudryavtsev *et al.*, 2013]. Using polarization decompositions and contrasts [Kudryavtsev *et al.*, 2014a], the background (wind dependent) properties can then be more efficiently separated from the local effects. Where ocean surface current gradients occur, CP signals also clearly depart from PD ones, confirming the large CP sensitivity to rougher areas and surface breakers. Today, polarization decompositions can further be applied over larger swath ocean scenes, with the Sentinel-1 A mission, the first of a two satellites

constellation carrying C-band SAR (C-SAR) instruments, capable to acquire dual polarization (VV + VH or HH + HV) signals.

To complement previous case studies and reported empirical relationships, we thus present and analyze global C-band ENVISAT and Sentinel-1 SAR measurements in copolarization and cross-polarization. Using colocated ancillary winds, such a global analysis at medium resolution (tens of kilometers) helps to especially document, for the first time, wind speed and direction sensitivity for HH measurements with respect to incidence angles. Subsequently, this enables to compare VV-derived and HH-derived geophysical model functions (GMFs), and to further analyze PD, PR, and CP signal properties. This allows to discuss quantitative interpretation of ocean-radar interactions to advance consistent inversion of ocean-atmosphere couplings at high resolution.

## 2. Data Set

C-band SAR data have been accumulated from ENVISAT ASAR for copolarization measurements, and from Sentinel-1 A and RS-2 for cross-polarization ones. Colocated ocean surface wind magnitudes and directions are ECMWF atmospheric model outputs and METOP/ASCAT scatterometer estimates. ECMWF 10 m winds are given at 0.125° every 3 h. We use ASCAT 12.5 km Level 2 wind products processed by KNMI using CMOD-5.n GMF. In this study, we do not attempt to derive wind speed nor wind direction from the SAR products.

### 2.1. Copolarized NRCS

ENVISAT/ASAR and METOP/ASCAT orbits and fields of view enable less than 1 h separation colocations. Intersecting areas are maximized for ASAR acquisitions in Wide Swath Mode (WSM), to cover about 400 km in the range direction and more than 1000 km along track. C-band NRCS incidence angles are from 16° to 42°. ASAR separately acquires VV or HH signals. As such, VV and HH ASAR measurements correspond to two different data sets.

All ASAR WSM products acquired in 2009 have been systematically processed to derive the NRCS, incidence and azimuth look angles at a resolution cell of 12.5 km, then colocated with ASCAT wind speed and direction. More than 2700 SAR images were considered, resulting in more than 150,000 and 250,000 colocations for VV and HH, respectively.

Prior to launch, the ASAR NESZ ( $n$ ) has been estimated by ESA for each WSM subswaths [European Space Agency, 2007]. The values (between  $-20$  and  $-30$  dB) can affect the NRCS at high incidence angles and low winds, especially for HH measurements. The NESZ can also be experimentally estimated. Indeed, considering all ocean surface NRCS at a resolution of 1 km, a clear noise floor corresponding to the envelope of the lowest NRCS values is obtained, showing different values for the different subswaths. A NESZ has then been monthly estimated for each polarization, and then subtracted from the NRCS:

$$\sigma_0^{pp}(\theta)|_{\text{clean}} = \sigma_0^{pp}(\theta) - n(\theta), \tag{1}$$

where the NRCS,  $\sigma_0^{pp}$  ( $pp$  stands for polarization) and the NESZ are expressed in linear units.  $\theta$  is the incidence angle.

As commonly formulated, a harmonic decomposition is considered:

$$\sigma_0^{pp}(\theta, \phi, u_{10}) = a_0^{pp}(\theta, u_{10}) [1 + a_1^{pp}(\theta, u_{10}) \cos(\phi) + a_2^{pp}(\theta, u_{10}) \cos(2\phi)], \tag{2}$$

where  $u_{10}$ ,  $\theta$ , and  $\phi$  stand for the wind speed, incidence angle, and wind direction relative to the radar azimuth look angle, respectively. Hereafter,  $\phi$  is called the azimuth angle,  $\phi=0^\circ$  and  $\phi=180^\circ$  are for upwind (wind is blowing toward the radar antenna) and downwind configurations, whereas  $\phi=90^\circ$  and  $\phi=270^\circ$  represent crosswind configurations. The first-order coefficient  $a_1^{pp}$  scales an upwind-downwind asymmetry. The second-order term  $a_2^{pp}$  scales the upwind-crosswind directionality.

For each incidence angle and wind speed bin, the NRCS is then analyzed as a function of  $\phi$  to determine the corresponding  $a_i^{pp}$  coefficients by regression. Figure 1 presents ASAR NRCS (black dots) for 7 m/s wind speed and 35° incidence angle. For each polarization, estimated NRCS using equation (2) are represented in blue in Figure 1.

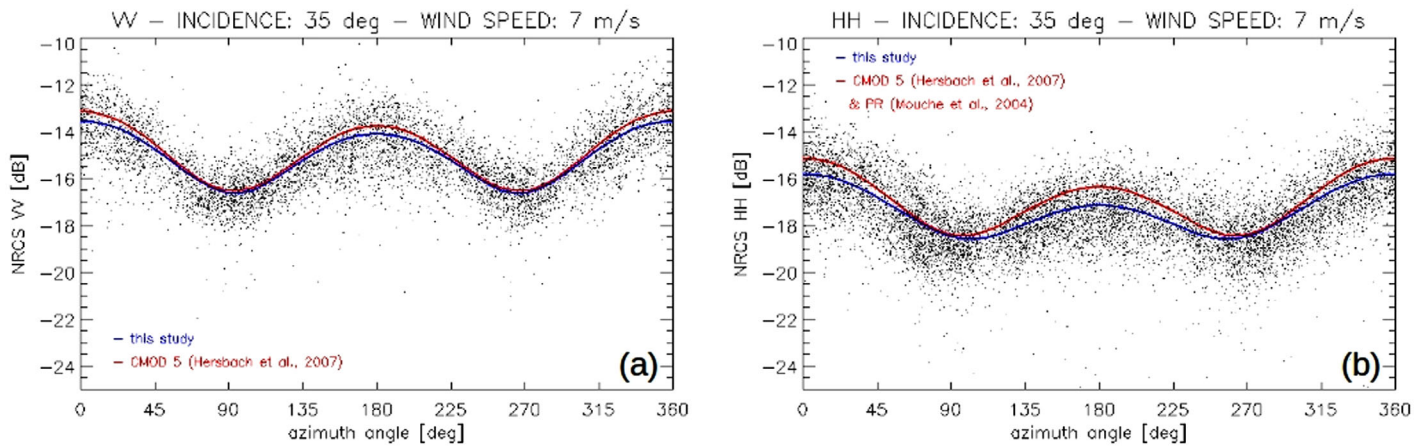


**Figure 1.** NRCS as a function of azimuth angle for a 7 m/s wind speed and 35° incidence angle. (a) VV and (b) HH. Black dots are NRCS measurements from ASAR. Blue line is the results of the regression. For VV polarization, the red line is the results given by CMOD-5 [Hersbach et al., 2007]. For HH, the results in red is given by CMOD-5 combined with the azimuth wind direction dependent PR proposed by Mouche et al. [2005].

For VV polarization, CMOD-5 model, in red, is in good agreement, to prove consistency between ASCAT and ASAR NRCS. Following Thompson et al. [1998], CMOD-5 is transformed to a HH GMF using the azimuth wind direction dependent polarization ratio (PR) model proposed by Mouche et al. [2005]. For this configuration ( $u_{10} = 7$  m/s and  $\theta = 35^\circ$ ), the CMOD-5 + PR model displays an overall good agreement, but the NRCS asymmetry with respect to the azimuth angle is less pronounced from the data analysis.

This has been performed for all bins of incidence angles and wind speeds, i.e., from 17° to 42° with a bin size of 1° and a bin step of 0.5°, and from 2 to 20 m/s with a bin size of 1 m/s and a bin step of 1 m/s. The  $\alpha_i^{pp}$  coefficients have been derived with and without taking into account the NESZ, leading to new C-band GMF (C-SARMOD) for both VV and HH, as given in Appendix A.

### 2.2. Cross-Polarized NRCS

For cross-polarized measurement, RS-2 and Sentinel-1 A [European Spatial Agency, 2014] data are considered. NESZ is different and available for each RadarSat-2 product, leading to relationships between wind speed for each acquisition mode. As reported, the so-called quad-polarization mode has the lowest NESZ.

In this study, 50 RS-2 products acquired in Fine Quad-Pol mode, processed up to Level-1 SLC by VIGISAT receiving station using the MDA processor have been considered for comparison with Sentinel-1 A measurements. NRCS are estimated at 12.5 km resolution, with and without applying the NESZ correction, and further collocated with ECMWF winds. In Fine Quad-Pol mode, swath is 50 km wide and covers incidence angles from 19° to 47°.

The C-SAR instrument on board Sentinel-1 A does not benefit from a quad-polarization mode with low values for NESZ but has two modes to enable dual-polarization measurements with large swaths: Extra Wide (EW) and Interferometric Wide (IW) swath modes. Dual polarization acquisitions are VV + VH or HH + HV. All Sentinel-1 A data acquired in cross-polarization presented hereafter have been obtained from EW and processed up to Level-1 FR GRD by ESA PDGS using Terrain Observation with Progressive Scans SAR (TOPSAR). EW swath is 400 km wide and covers incidence angles from 18° to 42°.

As for ASAR, the NESZ has also been estimated empirically from the data, using NRCS values at 1 km resolution. The NESZ as function of elevation angle for EW is presented in Figure 2c. The impact of the antenna gain on each of the five subswaths is clearly visible. NESZ ranges from -26 to -37 dB, decreasing with increasing incidence angle. Though the trend is opposite, between 25° and 47°, NESZ values are between -37 and -32 dB, close to reported values for RS-2 quad-polarization mode CP data [Vachon and Wolfe, 2011].

NRCS, elevation, incidence, and azimuth angles are then derived at a 12.5 km resolution cell and collocated with ECMWF wind speed and direction. The NRCS is corrected from the NESZ following equation (1). As obtained, NESZ significantly impacts the CP NRCS, especially for winds below 10 m/s (see Figures 2a and 2b).

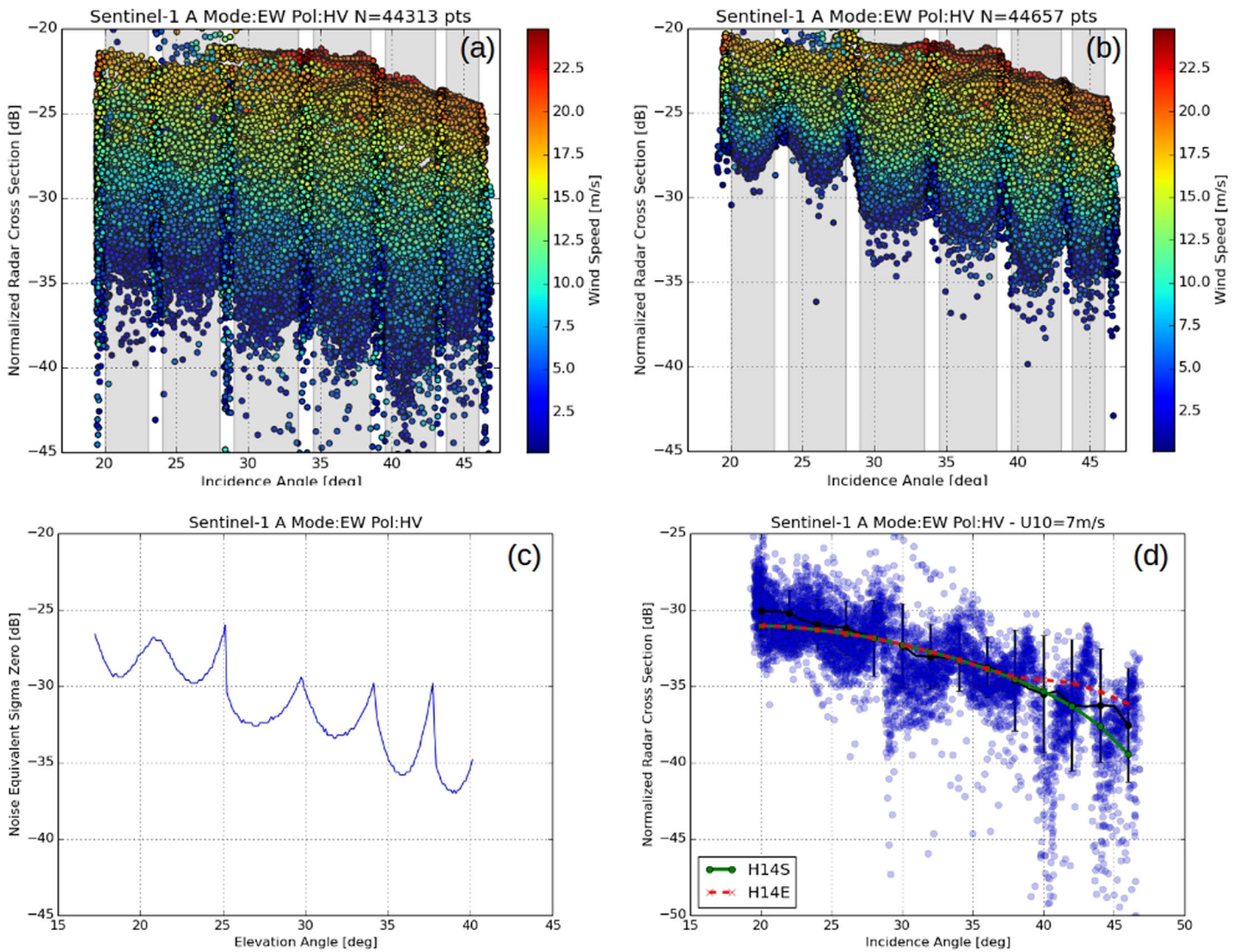


**Figure 2.** (a) NRCs in cross-polarization as a function of incidence angle as derived from Sentinel-1 A data acquired in EW mode over ocean, without taking into account for NESZ. (b) Same as Figure 2a but with correction for NESZ. (c) NESZ as a function of elevation angle as derived from Sentinel-1 A data acquired in EW mode over ocean. (d) Same as Figure 2b but for a 7 m/s wind speed. Red and green curves are from GMFs proposed by Hwang et al. [2015].

Consistent with reported RS-2 analysis [e.g., Hwang et al., 2015], CP NRCS slightly decreases (approximately 5 dB) with incidence angle from 19° to 47° (see Figure 2d), for moderate wind speeds.

### 3. Data Analysis

#### 3.1. Copolarization

To date C-band VV, through CMOD-suite [Stoffelen and Anderson, 1997; Quilfen et al., 1998; Hersbach et al., 2007], dominates the literature, especially to describe first-order NRCS sensitivity with respect to wind speed and direction [Quilfen et al., 1999], for operational wind retrieval with European C-band scatterometers. Despite routine C-band HH acquisitions, starting with RS-1, only ad hoc adjustments based on an a priori PR [Thompson et al., 1998] have been suggested to interpret such data in terms of wind. Yet Mouche et al. [2005] explicitly show a very salient feature of C-band backscatter measurements, i.e., for incidence angles larger than 30°, PR is consistently observed to be strongly wind direction dependent [see also Mouche et al., 2007b, Figure 5]. As reported, the C-band PR appears minimum for crosswind conditions, and maximum for downwind ones.

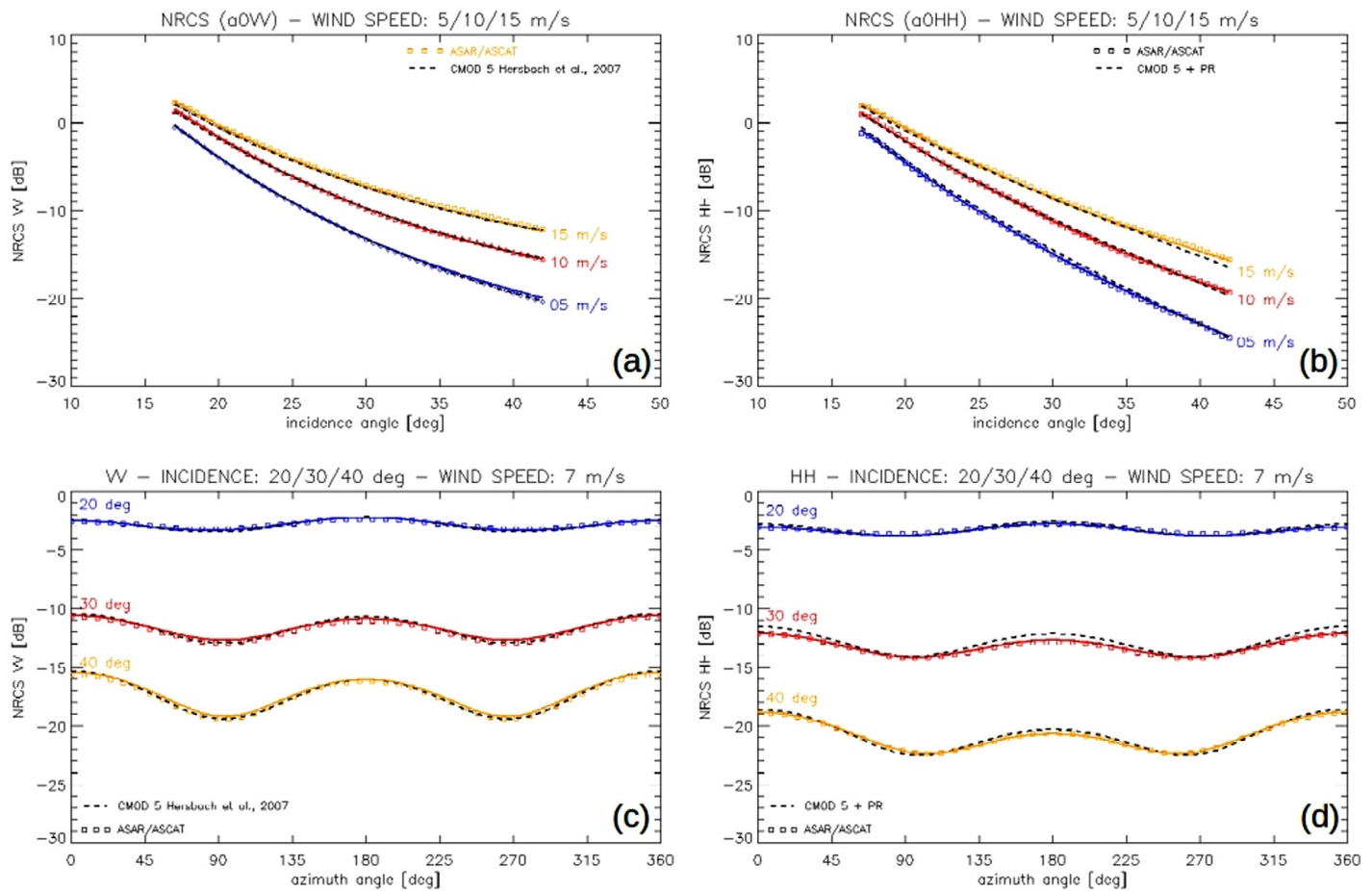


**Figure 3.** (top) NRCS ( $\alpha_0$ ) as a function of incidence angle for a 5, 10, and 15 m/s wind speed. (a) VV and (b) HH. Black dashed lines stand for CMOD-5 (VV) or CMOD-5 combined with PR (HH). (bottom) NRCS as a function of azimuth angle for a 20°, 30°, and 40° incidence angle for a 7 m/s wind speed. (a) VV and (b) HH. Black dashed lines stand for CMOD-5 (for VV) or CMOD-5 combined with PR (for HH). Squares stand for coefficients combination (using equation (2)) obtained from ASAR data analysis. Solid line is from SARMOD (see Annex for coefficients). We use the azimuth wind direction dependent polarization ratio from *Mouche et al.* [2005].

For VV polarization (see Figures 3a and 3c), the derived wind speed sensitivity and azimuth variation are very close to CMOD-5, validating the noise correction and calibration procedure with respect to the incidence angle. For HH, Figures 3b and 3d, an overall good agreement is found with the CMOD + PR adjustment, mostly departing for winds above 15 m/s and incidence angles larger than 35°. As obtained, PR thus decreases with increasing wind speed. This is further discussed in section 3.3.

### 3.2. Cross-Polarization

As understood, a particular polarization of the incident field in the observation frame of reference can be modified when referred to a local frame of reference that is tilted by the presence of long-scale facets. This modification will then depend on the in-plane and out-of-plane tilts. Considering the incident polarization to be either horizontal or vertical, when referred to the observation frame, the backscatter field becomes a mixture of both. For resonant centimeter scales over an untilted surface, the scattered field would not carry any depolarization. Yet because of the underlying tilting, the total backscatter may have cross-polarized components. As well, specular slopes shall not yield depolarized component. Thus, a tangent-plane approximation cannot apply to explain CP measurements. Yet from a finitely conducting random very rough surface, depolarization can still arise using a Physical Optics approximation that takes into account the modified local incidence angles at each point. For such an approximation, the local parallel and cross-polarized Fresnel coefficient related to the complex relative permittivity of the surface must be taken into account.

Figure 4 summarizes the CP NRCS with respect to wind speed. Analysis is performed for several ranges of incidence angles ((a) 20°–23°, (b) 24°–28°, (c) 29°–33.5°, (d) 34.5°–38.5°, (e) 39.5°–43.0°, and (f) 43.75°–46°)

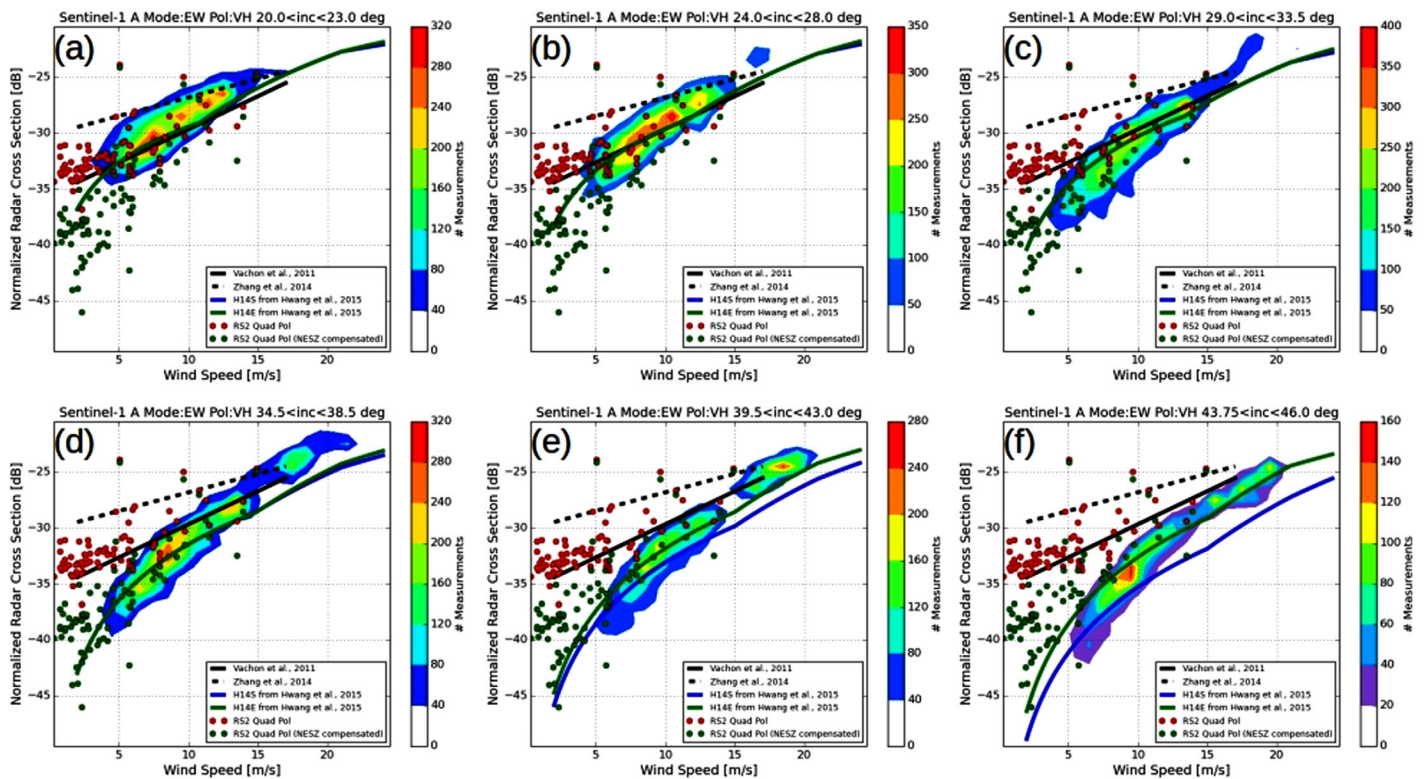


**Figure 4.** 2-D histogram of NRCS in cross-polarization as a function of wind speed for the six different subswaths of the Sentinel-1 A EW acquisition mode. Wind is provided by ECMWF analysis. Red and green dots are NRCS in cross-polarization from RadarSAT-2 respectively with and without correction from NESZ as given in the products. Green and blue lines are the results from GMF proposed by *Hwang et al.* [2015].

with respect to the Sentinel-1 EW subswaths, solely considering CP NRCS estimated in the middle of each subswath. The range of incidence angles considered for each subswath is indicated in light grey in Figures 2a and 2b. Consistent with documented RS-2 analysis, Sentinel-1 CP signals monotonically increase within the range of accumulated wind speeds. Also reported are empirical relationships proposed by *Vachon and Wolfe* [2011] for Quad-pol RS-2 data and *Hwang et al.* [2015] and *Zhang et al.* [2014] for RS-2 dual-pol data. Sentinel-1 A measurements are apparently closer to the relationship obtained with RS-2 quad-pol data. For each subswath, RS-2 quad-polarization data, with and without considering the NESZ are also presented. Without explicitly sorting them according to incidence angle, the considered RS-2 CP NRCS, corrected for available NESZ, are found to be very close to our analysis.

### 3.3. Polarization Combination

For the PR, results are presented in Figure 5. This analysis confirms major findings from previous studies. (i) The PR increases with increasing incidence angle, but at a significantly lower level than standard two-scale theories. (ii) The PR decreases with increasing wind speeds, in line with the results obtained using RS-2 data [e.g., *Zhang et al.*, 2011] or model [e.g., *Kudryavtsev et al.*, 2003; *Mouche et al.*, 2007a]. (iii) The azimuth modulation, as observed with airborne data [*Mouche et al.*, 2005], is also found, in line with model development [e.g., *Kudryavtsev et al.*, 2003; *Mouche et al.*, 2007b], reaching maximum value in downwind.

As anticipated [see also *Zhang et al.*, 2011], the absolute PR level is very sensitive to the NESZ. PR results derived from a set of  $a_i^{pp}$  coefficients derived with and without NESZ correction are shown in Figure 5c. As expected, the noise impacts measurements at large incidence angles and low wind speeds. Beyond these possible technical issues using C-band HH radar measurements, PR is an interesting quantity to possibly distinguish the polarized contributions from the total NRCS. Indeed, we can simply combine

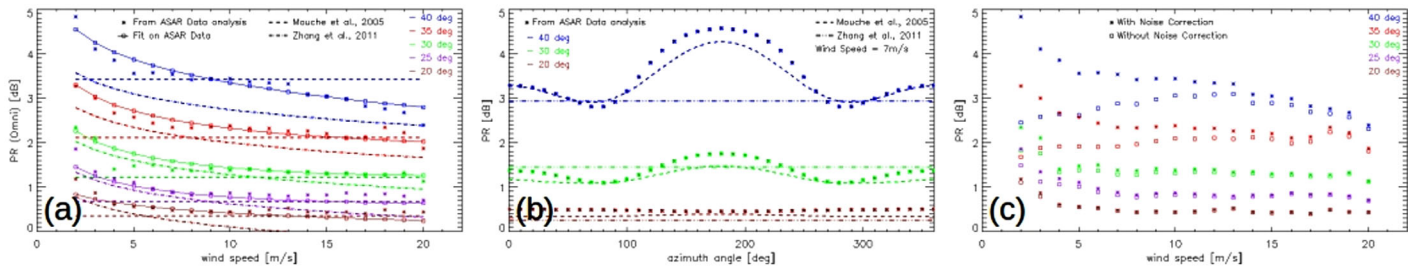


**Figure 5.** (a) Omnidirectional polarization ratio ( $a_0^{vv}/a_0^{hh}$ ) versus wind speed for various incidence angles. Stars stand for the analysis from joint ASCAT wind and ASAR NRCS. Solid lines with squares stand for the SARMOD model. Dashed and dashed-dotted lines are respectively from the empirical formulations proposed by *Mouche et al.* [2005] and *Zhang et al.* [2011]. The color code indicates the incidence angle (see legend). (b) Polarization ratio versus azimuth angle for various incidence angles. Stars stand for the analysis from joint ASCAT wind and ASAR NRCS. Dotted lines and dashed lines respectively stand for models proposed by *Mouche et al.* [2005] and *Zhang et al.* [2011] models. The color code indicates the incidence angle (see legend). (c) Polarization ratio versus wind speed for various incidence angles. Stars and squares respectively stand for the analysis from joint ASCAT wind and ASAR NRCS with and without NESZ correction.

$$PR(\theta, \phi, u_{10}) = 1 + \frac{\sigma_0^{vv}(\theta, \phi, u_{10}) - \sigma_0^{hh}(\theta, \phi, u_{10})}{\sigma_0^{hh}(\theta, \phi, u_{10})} = 1 + \frac{PD}{\sigma_0^{hh}(\theta, \phi, u_{10})}. \quad (3)$$

As already mentioned [e.g., *Kudryavtsev et al.*, 2013], PD mostly contains information about fast-response spatial changes of short-scale resonant Bragg waves, which are mainly caused by variable wind field and/or the presence of surface slicks. Contrasting PD and PR values, or equivalently PD and HH values, can then help to detect and quantitatively discriminate ocean surface roughness signatures. For instance, PD shall be weakly affected over surface current gradient areas, while  $\sigma_0^{hh}(\theta, \phi, u_{10})$  shall be responding to changes in the local distribution of breaking waves.

From this global analysis, the noteworthy difference between the azimuth modulation observed for PR, copolarized channels and PD, provides additional information on the azimuth distribution of nonpolarized and polarized scattering contributions [*Chapron et al.*, 1997; *Quilfen et al.*, 1999; *Mouche et al.*, 2006, 2007b]. In particular, the marked (and opposite in sign) up/downwind asymmetries obtained for the PR and PD, with maximum downwind PR values closer to a two-scale model prediction, suggest a strong anisotropy (upwind and downwind) for the shape and/or the distribution of non or weakly polarized scatters.

In Figure 6a, we present the PD omnidirectional component with respect to wind speed. It is defined as  $PD = a_0^{vv}(u_{10}) - a_0^{hh}(u_{10})$ . PD measures polarization sensitivity and best characterizes the resonant scattering mechanism mostly governed by centimeter-scale surface waves [*Mouche et al.*, 2007a; *Guérin et al.*, 2010]. Accordingly, PD azimuthal modulation can essentially be attributed to the directional distribution of short waves. Up-crosswind asymmetry (UCA) for both NRCS and PD is defined as

$$UCA^{PP}(\theta, U_{10}) = \frac{a_0^{pp} + a_2^{pp}}{a_0^{pp} - a_2^{pp}} - 1 \text{ [linear units]}, \quad (4)$$

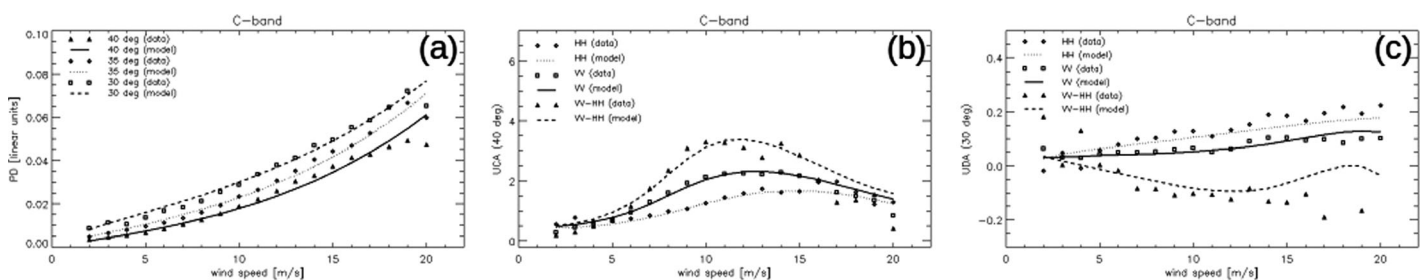


**Figure 6.** Polarization difference as function of wind speed for the omnidirectional component computed with  $a_0^{vv}$  and  $a_0^{hh}$  coefficients obtained with ENVISAT/ASAR measurements for three different incidence angles: 30°, 35°, and 40°. (b) Up-crosswind asymmetry for both copolarization channels and the difference of polarization (see equations (4) and (5)) as function of wind speed for a 40° incidence angle. (c) Up-downwind asymmetry for both copolarization channels and the difference of polarization (see equations (6) and (7)) as function of wind speed for a 30° incidence angle.

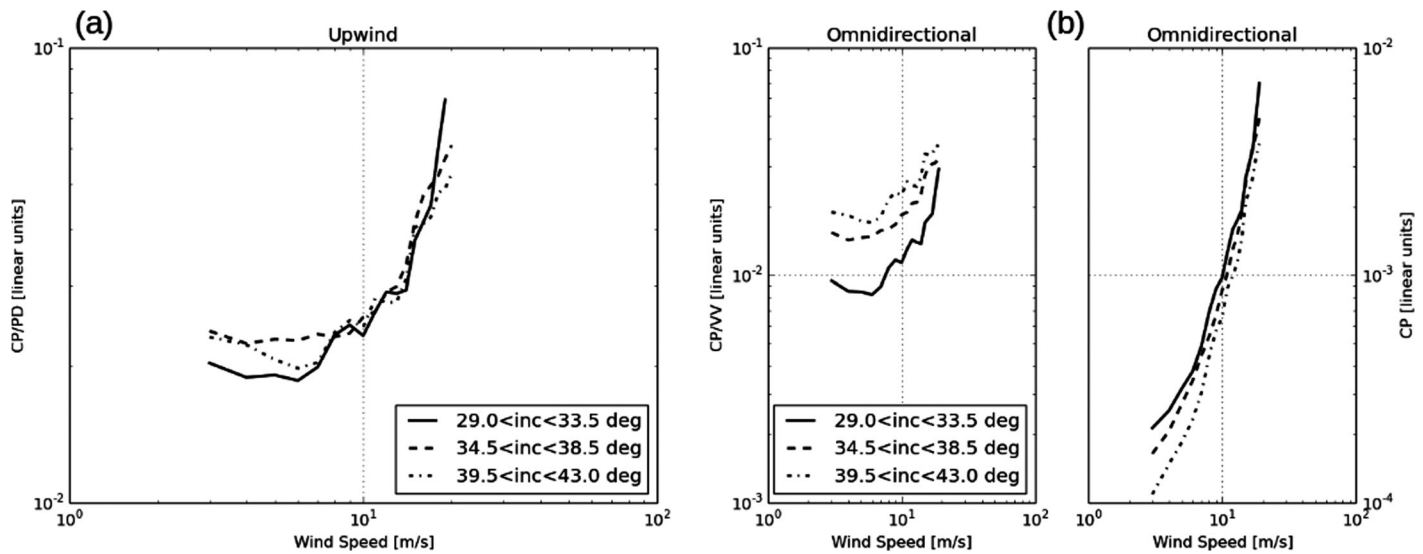


**Figure 7.** (a) CP/PD ratio as a function of wind speed for the omnidirectional component three ranges of incidence angles: 29.0°–33.5°, 34.5°–38.5°, and 39.5°–43.0°. PD is computed with  $a_0^{vv}$  and  $a_0^{hh}$  coefficients obtained with ENVISAT/ASAR measurements. CP is given by the fits in Figure 4.

$$UCA^{PD}(\theta, U_{10}) = \frac{(a_0^{vv} + a_2^{vv}) - (a_0^{hh} + a_2^{hh})}{(a_0^{vv} - a_2^{vv}) - (a_0^{hh} - a_2^{hh})} - 1 \quad [\text{linear units}]. \quad (5)$$

Figure 6b presents UCA for VV, HH, and PD as a function of wind speed at 40° incidence angle. As already reported for Ku-band [Quilfen *et al.*, 1999], C-band UCA is larger in VV than HH, and maximum for PD. As the HH nonpolarized contributions are likely to be relatively larger than VV ones, these contributions are thus less directional than resonant short scales. For PD, UCA behavior with respect to wind speed and incidence angle is very consistent with wave spectral measurements reported by Yurovskaya *et al.* [2013]. Yet for C-band, UCA increases up to 10 m/s to then saturate and decreases at higher winds. For Ku-band, peak directionality occurs around 8 m/s [see Quilfen *et al.*, 1999, Figure 6]. For both cases, this can be attributed to an increasing impact of the more isotropic nonpolarized contributions, likely associated with more vigorous and large-scale breaking occurrences. As such, from moderate to high winds, crosswind copolarized signals increase more rapidly than along-wind ones, especially for HH measurements.

The up-downwind asymmetry (UDA) is defined by

$$UDA^{PP}(\theta, U_{10}) = \frac{a_1^{pp}}{a_0^{pp}} \quad [\text{linear units}], \quad (6)$$

$$UDA^{PD}(\theta, U_{10}) = \frac{a_1^{vv} - a_1^{hh}}{a_0^{vv} - a_0^{hh}} \quad [\text{linear units}]. \quad (7)$$

Figure 6c presents UDA for VV, HH, and PD as a function of wind speed at 30° incidence angle. For VV and HH, C-band UDA is positive and increases with wind speed, with HH UDA larger than VV UDA. For PD, UDA is negative and decreases with increasing wind speed. As already pointed out for Ku-band [Chapron *et al.*, 1997], this indicates that the polarized resonant scattering mechanism is more effective downwind (windward waves) than upwind (leeward waves), i.e., windward short waves may be hypothesized to fulfill the small-perturbation criterion. The positive UDA for copolarization VV and HH measurements can thus be explained from the possible skewness of the tilting longer waves, and leeward surface roughness elements which cannot be treated as small-perturbation scatters, such as breakers. In such a case, the backscattering becomes nonpolarized to follow asymptotic Physical-Optics Kirchhoff mechanism. This assumption is underlying the model development proposed by Kudryavtsev *et al.* [2003].

Using this global analysis, we can further investigate the relationship between PD and CP. The ratio CP/PD is presented in Figure 7 as a function of wind speed for three ranges of incidence angles (29.0°–33.5°, 34.5°–38.5°, and 39.5°–43.0°) in omnidirectional configuration.

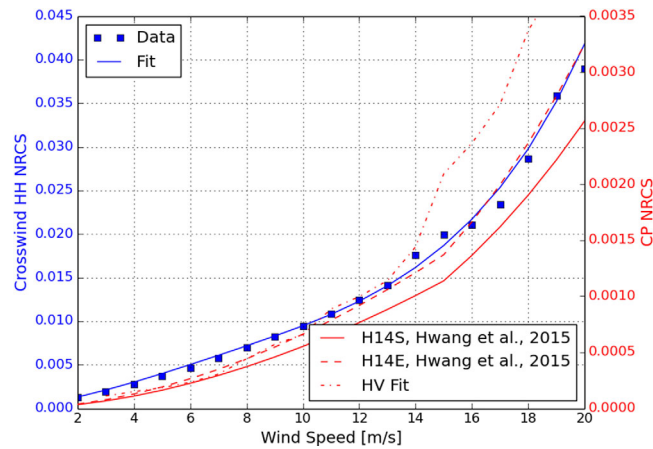


Figure 8. NRCS in HH for crosswind and NRCS in CP as a function of wind speed.

As reported by Kudryavtsev et al. [2014a] for only two cases, global relationships confirm close covariations between CP and PD under light to moderate wind conditions. Beyond 8–9 m/s, CP is then clearly found more responsive to wind speed change than PD. In line with UCA analysis, this threshold wind may well correspond to the onset of vigorous breaking events, large enough to directly impact C-band in-plane and out-of-plane local tilts. Accordingly, both nonpolarized and cross-polarized backscatter components would be enhanced. For particular cases, Kudryavtsev et al. [2014a] reported very significant CP/PD and PR

variations over strong surface current gradient areas, to demonstrate and quantitatively evaluate the relative impact of breakers on CP and PR signals. Although the process causing wave breaking is different, this is consistent with the present analysis, with a clear departure of CP/PD within the high wind speed regime.

Considering that HH polarization best minimizes the polarized resonant contribution, especially for crosswind conditions, it can be anticipated that both  $\sigma_0^{hh}(\theta, 90, u_{10})$  and CP shall exhibit comparable wind speed relationship, through a comparable sensitivity to breaking occurrence. Figure 8 effectively confirms such an intuitive analysis.

Moreover, it can be considered that VV polarization best maximizes the polarized resonant contribution. Accordingly, comparing CP and VV could be equivalent to compare  $\sigma_0^{hh}(\theta, 90, u_{10})$  and  $\sigma_0^{vv}(\theta, \phi, u_{10})$  and could trace and characterize local directional aspects. Such a potential somehow offers a surrogate azimuthal diversity to possibly constrain wind speed and direction retrieval methods, under single-antenna configuration. In that context, wide swath Sentinel-1 acquisitions shall possibly advance detailed analysis of wind-wave couplings, especially to better characterize directional aspects and breaking impacts [e.g., Kudryavtsev et al., 2014b] under different sea state degree of development.

#### 4. Conclusion

This paper presents an analysis of global C-band ENVISAT and Sentinel-1 SAR copolarized (VV and HH) and cross-polarized (CP) Sentinel-1 A measurements. Using colocated ancillary winds, this global analysis at medium resolution (tens of kilometers) helps to refine, especially for HH configuration, the wind speed sensitivity, and azimuthal variations for different incidence angles. As obtained, VV signals are very close to operational CMOD-5 GMF. For HH signals, the derived GMF is also consistent with previously proposed heuristic CMOD-5 + PR adjustment, mostly departing for winds above 15 m/s and incidence angles larger than 35°. In line with previous RS-2 measurements, the noise-corrected Sentinel-1 A CP measurements are incidence angle dependent for low to medium wind speeds, also increasing with no apparent saturation at high wind speeds.

Considering ocean-radar interactions, it still remains generally unclear whether the differences between theoretical calculations and experimental data should be attributed to deficiencies of the scattering model or to the inaccurate statistical description of the ocean surface roughness [Fois et al., 2015; Mouche et al., 2007a]. Yet the polarization sensitivity, such as the linear difference between VV and HH (PD), must trace the overall deviation of the ocean surface from its tangent-plane approximation over distances comparable to the radar wavelength. As such, PD is more directly governed by resonant scattering mechanism effects related to short and small amplitude surface centimeter scales. As mentioned, PD shall relax over short spatial scales (~10 m). PD contrasts can then often appear distinct compared to VV, HH, and also PR or CP ones.

Using the global analysis, this C-band polarization mean sensitivity is now documented. In particular, the depth of azimuthal modulation, measuring the wind directionality, is found larger for PD than copolarized

measurements. This can be mostly attributed to weak HH signals under crosswind conditions. As such, PR is also azimuthally distributed. Yet the PD depth of azimuthal modulation is not monotonically increasing with wind speed, peaking around 10 m/s. Beyond such a wind speed, the crosswind HH signals start to strongly increase, and PR values also decrease.

As compared, beyond this wind speed, crosswind HH NRCS exhibit a wind speed relationship comparable to CP measurements. While anticipated, this property has been overlooked over passed studies. As interpreted, HH polarized measurements generally minimize, compared to VV ones, the polarized short-scale resonant contribution. Thus, especially for crosswind configurations, HH signals shall be mostly sensitive to nonresonant scatters, likely associated with multiscale breakers. This can thus explain the high wind sensitivity of crosswind HH measurements. Vigorous breaking events, large enough to impact in-plane and out-of-plane local tilts, can indeed enhance both nonpolarized and cross-polarized backscatter components. For both HH, especially crosswind, and CP signals, out-of-plane tilts certainly strongly increase for winds above 10 m/s, to govern the electromagnetics and oceanic waves interactions.

As proposed, such a differing sensitivity between polarizing short-scale scatters and multiscale breakers shall thus be possibly further exploited when using contemporaneous VV and CP wide swath measurements, e.g., S-1 observations. As confirmed, VV measurements shall exhibit good directional sensitivity, larger than HH ones, while CP does not seem to be strongly wind direction dependent. Combined CP and VV signals can thus have the potential to map and contrast local directional aspects. As envisaged, such a combination somehow offers a surrogate azimuthal diversity to possibly constrain wind speed and direction retrieval methods, under single-antenna configuration. More generally, polarization decompositions can open practical strategies and essential means to resolve fine-scale atmospheric and oceanic features, as well as to quantitatively interpret and exploit the estimated overall polarized scatter line-of-sight velocity to advance detailed wind-wave-current information at high resolution. For the latter practical application, the global C-band NRCS analysis reveals different up-downwind asymmetries (UDAs). In particular, the PR and PD are larger for downwind observations compared to upwind ones. As interpreted, this likely indicates a more predominant impact of nonresonant scatters for upwind conditions. This helps to interpret the mean polarized Doppler absolute difference, i.e.,  $|\Delta f^{hh} - \Delta f^{vv}|$ , to be smaller for upwind than for downwind conditions [Mouche et al., 2012; Johannessen et al., 2008]. Future investigations will then be devoted to more closely analyze CP Doppler measurements to further help to better separate wind-wave-induced effects from surface current ones using combined CP and VV measurements.

### Appendix A: C-SARMOD, a GMF for VV and HH

As proposed, simple and analytical solutions in both HH and VV polarization are obtained to reproduce the behavior of the NRCS as observed by ASAR with respect of ASCAT winds. Thus, in the following,  $u_{10}$  stands for neutral winds. The NRCS  $\sigma_0^{pp}$  is expressed as a function of  $a_i^{pp}|_{i \in [0,2]}$  coefficients (see equation (2)). We used the constrain on the NRCS modulation with respect to azimuth angles between  $0^\circ$  and  $360^\circ$  to minimize the sample correlation.

Formula to calculate these coefficients are given below.

**Table A1.** Coefficients for  $\sigma_0^{pp}$

| $c_i^{pp}$ | $\ln G_{pp}$ | $H_{pp}$    | $\beta_{pp}$ |
|------------|--------------|-------------|--------------|
|            |              | HH          |              |
| 0          | -7.33139     | 1.03880     | 0.0762567    |
| 1          | -0.212909    | 0.0275352   | 0.00106068   |
| 2          | -0.000792705 | 0.00243772  | -0.000278180 |
| 3          | -0.000121630 | 7.47297E-05 | -6.44792E-06 |
|            |              | VV          |              |
| 0          | -6.16710     | 1.03880     | 0.0762567    |
| 1          | -0.146117    | 0.0275352   | 0.00106068   |
| 2          | 0.000551007  | 0.00243772  | -0.000278180 |
| 3          | -0.000104865 | 7.47297E-05 | -6.44792E-06 |

**Table A2.** Coefficients for  $a_1^{pp}$

|                     | VV                     |                        | HH                     |
|---------------------|------------------------|------------------------|------------------------|
| $\alpha^{pp}$       | +0.5494139875684466    |                        | +0.5578776236091342    |
| $\beta^{pp}$        | -0.2537941230194909    |                        | -0.1653473010020597    |
| $\lambda_{00}$      |                        | $+2.80 \times 10^{-2}$ |                        |
| $\lambda_{01}$      |                        | $+3.89 \times 10^{-2}$ |                        |
| $\lambda_{10}$      |                        | $-3.26 \times 10^{-1}$ |                        |
| $\lambda_{11}$      |                        | $+7.22 \times 10^{-2}$ |                        |
| $\gamma_0^{pp}$     | +2.837676553768251d+01 |                        | +8.509614426461971d+00 |
| $\gamma_1^{pp}$     | -6.082815686194667d+00 |                        | +1.085849816629014d+01 |
| $\gamma_2^{pp}$     | -7.355019708807264d+00 |                        | +1.229711688221634d+01 |
| $\gamma_3^{pp}$     | -2.120543368426278d+01 |                        | -3.254735774802430d+01 |
| $\gamma_4^{pp}$     | -9.996658491611458d+01 |                        | -2.000591131115483d+01 |
| $\omega_{0,0}^{pp}$ | -5.571007594704870d+00 |                        | -3.920637596874166d+00 |
| $\omega_{0,1}^{pp}$ | +7.077769998411096d-01 |                        | +2.253261536350614d+00 |
| $\omega_{0,2}^{pp}$ | +7.848179339751383d+00 |                        | +4.947185715842052d+00 |
| $\omega_{1,0}^{pp}$ | +5.172964892677770d+00 |                        | +2.145481327807399d+00 |
| $\omega_{1,1}^{pp}$ | -1.615631485131883d+00 |                        | +8.482177871475692d+00 |
| $\omega_{1,2}^{pp}$ | -7.280820027400687d+00 |                        | -2.565656541485563d+00 |
| $\omega_{2,0}^{pp}$ | +6.778888447797893d+00 |                        | -2.718527963841165d+00 |
| $\omega_{2,1}^{pp}$ | -6.190507136309122d+00 |                        | +8.741003943567796d-01 |
| $\omega_{2,2}^{pp}$ | -1.991751157336223d+00 |                        | +1.393783203709418d+00 |
| $\omega_{3,0}^{pp}$ | -6.628883243445240d+00 |                        | +1.572881607728977d+00 |
| $\omega_{3,1}^{pp}$ | +4.373479244934806d+00 |                        | +6.495185757622228d+00 |
| $\omega_{3,2}^{pp}$ | +1.145937393890187d+00 |                        | +5.134308584067237d-02 |

For  $a_0^{pp}$  coefficients, we simply adopted the methodology proposed by *Wentz and Smith* [1999] where  $a_0$  is expressed as

$$a_0^{pp} = G_{pp} u_{10}^{H_{pp}} \exp(\beta_{pp} u_{10}), \tag{A1}$$

and

**Table A3.** Coefficients for  $a_2^{pp}$

|                     | VV                     |                        | HH                     |
|---------------------|------------------------|------------------------|------------------------|
| $\alpha^{pp}$       | +7.277157636625426d-01 |                        | +5.760245557342257d-01 |
| $\beta^{pp}$        | -6.019084874008383d-02 |                        | -2.375070058873723d-02 |
| $\lambda_{00}$      |                        | $+2.80 \times 10^{-2}$ |                        |
| $\lambda_{01}$      |                        | $+3.89 \times 10^{-2}$ |                        |
| $\lambda_{10}$      |                        | $-3.26 \times 10^{-1}$ |                        |
| $\lambda_{11}$      |                        | $+7.22 \times 10^{-2}$ |                        |
| $\gamma_0^{pp}$     | -3.681506394149482d+00 |                        | -5.032548205859814d+00 |
| $\gamma_1^{pp}$     | -2.186451845911541d-01 |                        | +2.068851185351649d+01 |
| $\gamma_2^{pp}$     | +3.048209053057345d+00 |                        | -2.009344408396854d+01 |
| $\gamma_3^{pp}$     | -2.715551362070532d-01 |                        | -3.119093987614307d+01 |
| $\gamma_4^{pp}$     | +3.551950670620828d+00 |                        | +4.074073122851674d+01 |
| $\omega_{0,0}^{pp}$ | +1.475996489939081d+01 |                        | -2.946121186405037d+00 |
| $\omega_{0,1}^{pp}$ | +8.880426905679307d+00 |                        | +5.572302551252629d+00 |
| $\omega_{0,2}^{pp}$ | +2.164690118527864d+01 |                        | +6.194451729590362d-01 |
| $\omega_{1,0}^{pp}$ | +2.822253229212421d+00 |                        | +1.052888678131375d+00 |
| $\omega_{1,1}^{pp}$ | -6.346114276749153d+00 |                        | +2.506151601498831d-01 |
| $\omega_{1,2}^{pp}$ | +2.287031414332022d+00 |                        | -8.523957100277972d-01 |
| $\omega_{2,0}^{pp}$ | -1.280324647755258d+01 |                        | -8.711047499636486d-01 |
| $\omega_{2,1}^{pp}$ | -1.453828006545915d+01 |                        | -1.262081724670520d+00 |
| $\omega_{2,2}^{pp}$ | -2.499173464739155d+01 |                        | +1.565971116660313d+00 |
| $\omega_{3,0}^{pp}$ | -6.559782299569693d+00 |                        | +9.303838377811393d-01 |
| $\omega_{3,1}^{pp}$ | +1.075459789027327d+01 |                        | -3.018532968149969d+00 |
| $\omega_{3,2}^{pp}$ | +3.230573667664541d+00 |                        | +7.108209467344261d-01 |

**Table A4.** VV-Normalized Radar Cross Section  $\sigma_0^{vv}$  in dB for Several Values of Incidence Angles  $\theta$  (20°, 30°, and 40°), Wind Speeds  $u_{10}$  (5, 10, 15, and 25 m/s), and Azimuth Angles  $\phi$  (0 for Upwind, 90 for Crosswind, and 180 for Downwind)

| $\sigma_0^{vv}$ (dB) |           |           |          |          |          |          |          |          | $\theta$ (°) $\phi$ (°)<br>$u_{10}$ (m/s) |
|----------------------|-----------|-----------|----------|----------|----------|----------|----------|----------|---|
| 20°                  |           |           | 30°      |          |          | 40°      |          |          |   |
| 0                    | 90        | 180       | 0        | 90       | 180      | 0        | 90       | 180      |   |
| -3.60307             | -4.47923  | -3.37323  | -12.3314 | -14.0384 | -12.6134 | -17.6740 | -20.4710 | -18.3090 | 5 m/s                                     |
| -1.27837             | -2.27048  | -0.865463 | -8.29056 | -11.5317 | -8.63159 | -12.7032 | -17.8521 | -13.3450 | 10 m/s                                    |
| 0.455426             | -1.66054  | 0.974880  | -5.44088 | -9.63651 | -6.00640 | -9.37276 | -14.8143 | -10.2793 | 15 m/s                                    |
| 1.39686              | -0.839736 | 1.94487   | -3.50633 | -6.97612 | -4.31141 | -7.11298 | -11.1964 | -7.72289 | 20 m/s                                    |

**Table A5.** HH-Normalized Radar Cross Section  $\sigma_0^{hh}$  in dB for Several Values of Incidence Angles  $\theta$  (20°, 30°, and 40°), Wind Speeds  $u_{10}$  (5, 10, 15, and 25 m/s), and Azimuth Angles  $\phi$  (0 for Upwind, 90 for Crosswind, and 180 for Downwind)

| $\sigma_0^{hh}$ (dB) |          |          |          |          |          |          |          |          | $\theta$ (°) $\phi$ (°)<br>$u_{10}$ (m/s) |
|----------------------|----------|----------|----------|----------|----------|----------|----------|----------|---|
| 20°                  |          |          | 30°      |          |          | 40°      |          |          |   |
| 0                    | 90       | 180      | 0        | 90       | 180      | 0        | 90       | 180      |   |
| -4.12289             | -5.10649 | -3.99293 | -13.9812 | -15.7970 | -14.4465 | -21.3045 | -23.9954 | -22.9843 | 5 m/s                                     |
| -1.66649             | -2.69744 | -1.30146 | -9.73620 | -12.6065 | -10.4511 | -15.9368 | -20.2483 | -17.6934 | 10 m/s                                    |
| 0.283762             | -2.06168 | 0.620279 | -6.65707 | -10.7856 | -7.57664 | -12.3140 | -17.2903 | -13.8794 | 15 m/s                                    |
| 1.44549              | -1.30857 | 1.66728  | -4.52247 | -8.46526 | -5.65407 | -9.70081 | -13.7912 | -10.9861 | 20 m/s                                    |

$$X_p = \sum_{i=0}^3 c_i^{pp} (\theta - 40)^i, \quad (A2)$$

where  $X_p$  stands for  $\ln G_{pp}$ ,  $H_{pp}$ , and  $\beta_{pp}$ . Coefficients are summarized in Table A1.

For  $a_1^{pp}$  and  $a_2^{pp}$  coefficients, we choose the following approach:

$$a_{1,2}^{pp} = \alpha^{pp} F[\gamma(\theta, u_{10}, pp)] + \beta^{pp}, \quad (A3)$$

where the generic function  $F(\xi)$  is defined as

$$F(\xi) = \frac{1}{1 + e^{-\xi}}, \quad (A4)$$

$$Y(\theta, u_{10}, pp) = \gamma_0^{pp} + \sum_{i=1}^4 \gamma_i^{pp} F[\Gamma_{i-1}^{pp}(\theta, u_{10})], \quad (A5)$$

where

$$\Gamma_k^{pp}(\theta, u_{10}) = \omega_{k,0}^{pp} + \omega_{k,1}^{pp} V_1(u_{10}) + \omega_{k,2}^{pp} V_2(\theta) |_{k \in [0,3]}, \quad (A6)$$

$$V = \begin{pmatrix} V_1 \\ V_2 \end{pmatrix} = \begin{pmatrix} \lambda_{01} + \theta \lambda_{00} \\ \lambda_{11} + u_{10} \lambda_{10} \end{pmatrix}. \quad (A7)$$

#### Acknowledgments

This paper has been possible thanks to SAR data access granted by GIS Bretel, Sentinel-1 A Mission Performance Center (4000107360/12/I-LG), and Wind/Waves/Currents (18709/05/I-LG) ESA projects. Copernicus Sentinel data (2014, 2015) were used for this study. RADARSAT-2 data are from the Canadian Space Agency (CSA). ECMWF winds are produced by ECMWF and the access was obtained in the framework of Wind/Waves/Currents (18709/05/I-LG) ESA project. ASCAT Level-2 products are processed by KNMI and freely available. See their website: <http://projects.knmi.nl/scatterometer/>.

Coefficients are summarized in Tables A2 and A2.

Numerical results obtained with this GMF are given in Table A4 for VV and in Table A5 for HH, for users to test their implementation. They are presented in dB, i.e.,  $\sigma_0 = 10 \log_{10}(\text{SARMOD}(\theta, u_{10}, \phi))$ .

#### References

- Alpers, W., A. Mouche, J. Horstmann, A. Y. Ivanov, and V. S. Barabanov (2015), Application of a new algorithm using Doppler information to retrieve complex wind fields over the Black Sea from ENVISAT SAR images, *Int. J. Remote Sens.*, 36(3), 863–881.
- Chapron, B., V. Kerbaol, and D. Vandermark (1997), A note on relationships between sea-surface roughness and microwave polarimetric backscatter measurements: Results from POLRAD'96, in *Proceedings of the International Workshop POLRAD'96*, pp. 55–64, ESA Communications, ESTEC, Noordwijk, Netherlands.
- Chapron, B., F. Collard, and F. Ardhuin (2005), Direct measurements of ocean surface velocity from space: Interpretation and validation, *J. Geophys. Res.*, 110, C07008, doi:10.1029/2004JC002809.

- European Space Agency (2007), *ASAR Product Handbook*. Issue 2.2, ESRIN, Frascati, Italy.
- European Spatial Agency (2014), *Sentinel-1 User Handbook*, GMES-S1OP-EOPG-TN-13-0001, ESRIN, Frascati, Italy. [Available at <http://sentinel.esa.int>.]
- Fois, F., P. Hoogeboom, F. L. Chevalier, and A. Stoffelen (2015), An analytical model for the description of the full-polarimetric sea surface Doppler signature, *J. Geophys. Res. Oceans*, *120*, 988–1015, doi:10.1002/2014JC010589.
- Guérin, C.-A., G. Soriano, and B. Chapron (2010), The weighted curvature approximation in scattering from sea surfaces, *Waves Random Complex Media*, *20*(3), 364–384, doi:10.1080/17455030903563824.
- Hersbach, H., A. Stoffelen, and S. de Haan (2007), An improved Cband scatterometer ocean geophysical model function: CMOD5, *J. Geophys. Res.*, *112*, C03006, doi:10.1029/2006JC003743.
- Hwang, P. A., B. Zhang, and W. Perrie (2010a), Depolarized radar return for breaking wave measurement and hurricane wind retrieval, *Geophys. Res. Lett.*, *37*, L01604, doi:10.1029/2009GL041780.
- Hwang, P. A., B. Zhang, J. V. Toporkov, and W. Perrie (2010b), Comparison of composite Bragg theory and quad-polarization radar backscatter from RADARSAT2: With applications to wave breaking and high wind retrieval, *J. Geophys. Res.*, *115*, C08019, doi:10.1029/2009JC005995.
- Hwang, P. A., A. Stoffelen, G.-J. Van Zadelhoff, W. Perrie, B. Zhang, H. Li, and H. Shen (2015), Cross-polarization geophysical model function for C-band radar backscattering from the ocean surface and wind speed retrieval, *J. Geophys. Res. Oceans*, *120*, 893–909, doi:10.1002/2014JC010439.
- Johannessen, J. A., B. Chapron, F. Collard, V. N. Kudryavtsev, A. Mouche, D. Akimov, and K.-F. Dagestad (2008), Direct ocean surface velocity measurements from space: Improved quantitative interpretation of ENVISAT ASAR observations, *Geophys. Res. Lett.*, *35*, L22608, doi:10.1029/2008GL035709.
- Kudryavtsev, V., I. Kozlov, B. Chapron, and J. A. Johannessen (2014a), Quad-polarization SAR features of ocean currents, *J. Geophys. Res. Oceans*, *119*, 6046–6065, doi:10.1002/2014JC010173.
- Kudryavtsev, V., B. Chapron, and V. Makin (2014b), Impact of wind waves on the air-sea fluxes: A coupled model, *J. Geophys. Res. Oceans*, *119*, 1217–1236, doi:10.1002/2013JC009412.
- Kudryavtsev, V. N., D. Hauser, G. Caudal, and B. Chapron (2003), A semi-empirical model of the normalized radar cross section of the sea surface: 1. Background model, *J. Geophys. Res.*, *108*(C3), 8054, doi:10.1029/2001JC001003.
- Kudryavtsev, V. N., B. Chapron, A. G. Myasoedov, F. Collard, and J. A. Johannessen (2013), On dual co-polarized SAR measurements of the ocean surface, *IEEE Geosci. Remote Sens. Lett.*, *10*(4), 761–765.
- Lin, C., M. Betto, M. B. Rivas, A. Stoffelen, J. de Kloe (2012), EPS-SG windscatterometer concept tradeoffs and wind retrieval performance assessment, *IEEE Trans. Geosci. Remote Sens.*, *50*(7), 2458–2472, doi:10.1109/TGRS.2011.2180393.
- Mouche, A., B. Chapron, N. Reul, and F. Collard (2008), Predicted Doppler shifts induced by ocean surface wave displacements using asymptotic electromagnetic wave scattering theories, *Waves Random Complex Media*, *18*(1), 185–196.
- Mouche, A. A., D. Hauser, J.-F. Daloze, and C. Guérin (2005), Dual-polarization measurements at C-band over the ocean: Results from airborne radar observations and comparison with ENVISAT ASAR data, *IEEE Trans. Geosci. Remote Sens.*, *43*(4), 753–769.
- Mouche, A. A., D. Hauser, and V. N. Kudryavtsev (2006), Radar scattering of the ocean surface and sea-roughness properties: A combined analysis from dual-polarizations airborne radar observations and models in C band, *J. Geophys. Res.*, *111*, C09004, doi:10.1029/2005JC003166.
- Mouche, A. A., B. Chapron, and N. Reul (2007a), A simplified asymptotic theory for ocean surface electromagnetic wave scattering, *Waves Random Complex Media*, *17*(3), 321–341.
- Mouche, A. A., B. Chapron, N. Reul, D. Hauser, and Y. Quilfen (2007b), Importance of the sea surface curvature to interpret the normalized radar cross section, *J. Geophys. Res.*, *112*, C10002, doi:10.1029/2006JC004010.
- Mouche, A. A., F. Collard, B. Chapron, K.-F. Dagestad, G. Guitton, J. A. Johannessen, V. Kerbaol, and M. H. Hansen (2012), On the use of Doppler shift for sea surface wind retrieval from SAR, *IEEE Trans. Geosci. Remote Sens.*, *50*(7), 2901–2909, doi:10.1109/TGRS.2011.2174998.
- Quilfen, Y., B. Chapron, T. Elfouhaily, K. Katsaros, and J. Tournaire (1998), Observation of tropical cyclones by high-resolution scatterometry, *J. Geophys. Res.*, *103*(C4), 7767–7786, doi:10.1029/97JC01911.
- Quilfen, Y., B. Chapron, A. Bentamy, J. Gourrion, T. Elfouhaily, and D. Vandemark (1999), Global ERS-1/2 and NSCAT observations: Upwind/crosswind and upwind/downwind measurements, *J. Geophys. Res.*, *104*(C5), 11,459–11,470, doi:10.1029/1998JC000113.
- Quilfen, Y., C. Prigent, B. Chapron, A. Mouche, and N. Houti (2007), The potential of QuikSCAT and WindSat observations for the estimation of sea surface wind vector under severe weather conditions, *J. Geophys. Res.*, *112*, C09023, doi:10.1029/2007JC004163.
- Stoffelen, A. C. M., and D. L. T. Anderson (1997), Scatterometer data interpretation: Derivation of the transfer function CMOD4, *J. Geophys. Res.*, *102*(C3), 5767–5780, doi:10.1029/96JC02860.
- Thompson, D. R., T. Elfouhaily, and B. Chapron (1998), Polarization ratio for microwave backscattering from ocean surface at low to moderate incidence angles, paper presented at IEEE International Proceedings on Geoscience and Remote Sensing Symposium, IEEE, Seattle, Wash.
- Vachon, P. W., and J. Wolfe (2011), C-band cross-polarization wind speed retrieval, *IEEE Geosci. Remote Sens. Lett.*, *8*(3), 456–459, doi:10.1109/LGRS.2010.2085417.
- Wentz, F. J., and D. K. Smith (1999), A model function for the ocean-normalized radar cross section at 14 GHz derived from NSCAT observations, *J. Geophys. Res.*, *104*(C5), 11,499–11,514, doi:10.1029/98JC02148.
- Yurovskaya, M. V., V. A. Dulov, B. Chapron, and V. N. Kudryavtsev (2013), Directional short wind wave spectra derived from the sea surface photography, *J. Geophys. Res. Oceans*, *118*, 4380–4394, doi:10.1002/jgrc.20296.
- Zhang, B., and W. Perrie (2012), Cross-polarized synthetic aperture radar: A new potential technique for hurricanes, *Bull. Am. Meteorol. Soc.*, *93*, 531–541, doi:10.1175/BAMS-D-11-00001.1.
- Zhang, B., W. Perrie, and Y. He (2011), Wind speed retrieval from RADARSAT2 quad-polarization images using a new polarization ratio model, *J. Geophys. Res.*, *116*, C08008, doi:10.1029/2010JC006522.
- Zhang, B., W. Perrie, J. A. Zhang, E. W. Uhlhorn, and Y. He (2014), High-resolution hurricane vector winds from C-band dual-polarization SAR observations, *J. Atmos. Oceanic Technol.*, *31*(2), 272–286.